J. Micromech. Microeng. 4 (1994) 116–122. Printed in the UK

Post buckling of micromachined beams

W Fang and J A Wickert

Department of Mechanical Engineering, Carnegie Mellon University, Pittsburgh, PA 15213, USA

Received 21 February 1994, accepted for publication 4 August 1994

Abstract. The static deformation of micromachined beams under prescribed in-plane compressive stress is studied through analytical and experimental means over the prebuckling, transition, and postbuckling load ranges. The finite amplitude of the beam in its postbuckled state is predicted by modeling the non-linear dependence of the out-of-plane deformation on the compressive stress. In addition, the model explicitly considers the net effect of slight imperfections, which can include fabrication defects, geometric irregularities, or non-ideal loading, on the beam's behavior in the near-buckling regime. As an application, clamped–clamped silicon dioxide beams are fabricated through conventional bulk micromachining, and their deflected profiles are measured through three-dimensional optical profilometry. The measurements are compared to the postbuckled amplitudes and shapes that are predicted by the model, and by existing simpler models that do not include the effects of either non-linearity or imperfection. As borne out by the data, when imperfections are considered, the beams exhibit continuous growth of the out-of-plane amplitude during transition from the prebuckled state to a postbuckled one, in contrast to sudden bifurcation at a critical load. By accounting for this behavior, the estimate of residual stress in the thin film from which the beams are fabricated can be improved, and the amplitude of common postbuckled micromachined structures can be predicted during the design phase.

1. Introduction

Thin-film materials are used extensively in the areas of microelectronics, sensors, and actuators for their electrical, magnetic, and optical properties. The mechanical behavior of thin films is also relevant in the design process [1], and the consideration of fracture toughness, elastic modulus, and residual stress contributes to ensuring the reliability and functionality of microfabricated devices in harsh environments. For instance, excessive residual stress can cause failures through the blistering, peeling, or buckling of an insulating film [2], and in the case of a magnetostrictive material, magnetic properties couple with residual stress [3]. This latter phenomenon becomes of concern when high-performance magnetic media and recording heads are fabricated. In short, methods for measuring residual stress, and models for interpreting those measurements, frame a generic problem in the use of thin-film materials.

Several factors, including fabrication defects, contribute to the stress field in a thin film. In such processes as chemical vapor deposition and sputtering, the intrinsic stresses are not readily relaxed through either recovery or recrystallization mechanisms since the corresponding process temperatures are low when compared to the film's melting point [4]. When processing at high temperature is involved, for instance during thermal growth, the stress σ generated by the mismatch $\Delta\alpha$ of expansion coefficients between the film and its substrate can be significant. In the simple uniaxial case, the thermal strain is given by

$$\varepsilon = \frac{\sigma}{E} = \Delta T \, \Delta\alpha \qquad (1)$$

where E is the film's elastic modulus. Since the temperature change ΔT in some microfabrication processes is substantial, and because the expansion coefficients are somewhat temperature dependent, the averaging of $\Delta\alpha$ over the process range can provide an improved estimate of σ. While $\Delta\alpha$ might not be known *a priori* for the materials of interest, it can be measured indirectly by determining ε in a test structure.

Within the context of micromechanical systems, several approaches have been developed for determining stresses in thin films. With *in situ* techniques, the geometry of particular micromachined structures and their deformation under stress loading are measured, and σ is determined subsequently through a model of the test structure's elastic deformation. Arrays of clamped–clamped microbeams of different lengths have been used to determine stresses in polysilicon films [5, 6], and similar techniques have been applied to thermal SiO_2 [7, 8]. Alternative test structures, including cantilevers, membranes, and rings, have been examined in a similar vein [9, 10, 11].

In the case of micromachined beams, available models are based on the linear theory, so the stress

0960-1317/94/030116+07$19.50 © 1994 IOP Publishing Ltd

is found by identifying the beam of critical length L_c that demarcates the shorter (unbuckled) beams in the test array from the longer (postbuckled) ones. With L_c being known, classical Euler buckling analysis predicts the strain

$$\varepsilon = \frac{\pi^2 h^2}{3L_c^2} \tag{2}$$

where h is the thickness of the film from which the beam is fabricated. This analysis provides the strain level at which an experimental structure will begin to exhibit significant transverse deflection. On the other hand, it does not predict the amplitude of deformation, which can be of the order of several beam thicknesses, either near the buckling point or in the postbuckling regime.

In addition, transverse deflections of beams with lengths near (but below) L_c are observed experimentally, and yet are not predicted by the model as discussed. Such deflections are attributed to the small imperfections that are present in all real structures and which can arise from fabrication defects, geometric irregularities, or non-ideal loading [12]. For that reason, the distinction between 'unbuckled' and 'buckled' beams in the test array, namely the task of identifying L_c, can become blurred. Errors in measuring L_c, arising either from imperfections or simply from the finite number of beams in the array, propagate in equation (2) according to

$$\frac{d\varepsilon}{\varepsilon} = -2\frac{dL}{L} \tag{3}$$

and so the measured fractional error in L_c doubles when ε is determined through the simple model of equation (2).

In the present study, the effects of both non-linearity and imperfection are explicitly considered in the stress/deformation model, and the results are applied to the postbuckling of clamped–clamped micromachined beams under residual thermal stress. Measurements of deflected beam profiles demonstrate a continuous and monotonic growth of amplitude during transition from the prebuckled state to a postbuckled one. The residual stress, the level of imperfection in the micromachined beams, and a geometric constant are determined through a least-squares fit of the model to the measured data. With the model and experimental technique, the residual stress in the thin film from which the beams are fabricated can be estimated with greater precision, and the amplitude of the postbuckled micromachined structures can be predicted at the design stage.

2. Modeling and analysis

Buckling models are categorized as being linear (small deformation relative to the thickness of the structure) or non-linear, and as being based on perfect structures (idealized geometry and loading) or ones with slight imperfections (as are realized experimentally). The loss of stability of an idealized elastic structure in its 'prebuckled' state occurs through bifurcation into a 'postbuckled' equilibrium. The classical analysis for the

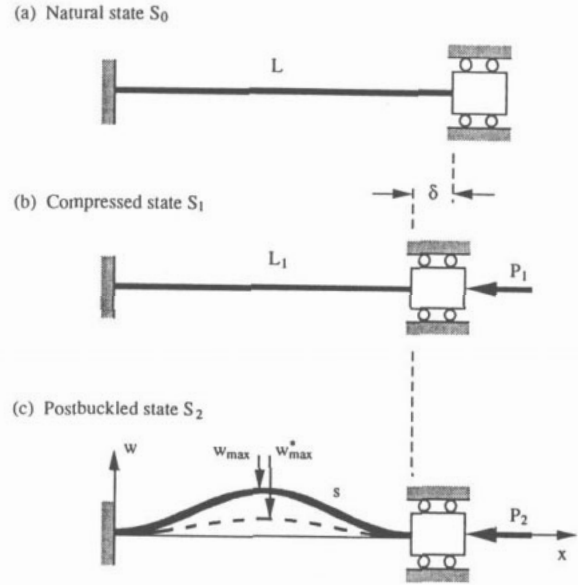

Figure 1. Loading of a micromachined beam in uniaxial compression. (a) The natural unstressed configuration, (b) the beam as compressed by a prescribed end displacement, and (c) the postbuckled state.

stability of the prebuckled state of a perfect structure reduces to an eigenvalue problem, and its solution provides the lowest load level P_c for which stability is lost and the shape w for initial postbuckling. The amplitude w_{max} of that deformation, however, remains undetermined in the linear theory.

The model problem considered here corresponds to a micromachined beam that is subjected to uniaxial compression; this situation arises, for instance, when oxide is thermally grown on silicon and has application to, for instance, certain high-sensitivity pressure sensors. Figure 1 illustrates a sequence of three states in the beam's loading process: the unstressed condition S_0, the straight configuration S_1 with uniaxial compression, and the postbuckled state S_2 in which fabricated structures are characterized experimentally. In S_0, the film is as grown at high temperature, and the beam has length L. The film and substrate in S_1 have cooled to room temperature, so as to compress the beam by amount δ to length L_1 as shown in figure 1(b) and impose the strain $\varepsilon = \delta/L$. At this stage, the beam has compression P_1, but no out-of-plane deformation has yet occurred. In S_2, the beam has been released from the substrate, and it has deflected with shape w. The end load does no work during transition from S_1 to S_2 because both of the beam's end-points remain fixed. Therefore, the strain energy in S_2 that is stored in compression and bending equals the energy in S_1 that was stored entirely in compression. Therefore, $P_2 < P_1$ as a result of the beam stretching under finite deformation.

Within the context of Euler–Bernoulli theory, the micromachined beam is modeled with flexural rigidity EI, axial stiffness EA, and clamped supports. In figure 1(c), the arc length is

$$s = L_1 + \frac{1}{2}\int_0^{L_1} w_{,x}^2 \, dx \tag{4}$$

where the comma subscript indicates differentiation, and is accurate to second order in w. The decrease of length in S_2 relative to S_0 is

$$\Delta s = \delta - \frac{1}{2}\int_0^{L_1} w_{,x}^2 \,\mathrm{d}x. \tag{5}$$

To the extent that the axial strain remains sufficiently small to be treated as linear, the load in the postbuckled state is given by

$$P_2 = EA\left(\varepsilon - \frac{1}{2L}\int_0^{L_1} w_{,x}^2 \,\mathrm{d}x\right). \tag{6}$$

Accurate to first-order changes in length, the domain of integration can be changed to L, and the governing equation for postbuckled deflection becomes

$$EIw_{,xxxx} + EA\left(\varepsilon - \frac{1}{2L}\int_0^{L} w_{,x}^2 \,\mathrm{d}x\right)w_{,xx} = 0 \tag{7}$$

subject to the conditions $w = w_{,x} = 0$ at $x = 0$ and L.

Imperfections are included next in order to describe the buckling behavior at near-critical δ (or for specified ε, near-critical L). Sources of imperfection can include stress variation through the film's thickness, curvature of the wafer, slight changes in the beam's cross-section along its length, or such external out-of-plane loads as electrostatic or surface tension forces. In each case, the effects of imperfection on the structure's deformation, particularly in the early postbuckling regime, are qualitatively similar. That is, initial imperfections render $w \neq 0$ when $L < L_c$, and the buckling amplitude grows smoothly during transition from the prebuckling region to the postbuckling one. This observation suggests that in the first approximation imperfections can be 'grouped' so that their net effect is represented by a single parameter in the model. To account for the physical effects of imperfections without the model becoming overwhelmed by the many contributing sources, the net imperfection is treated here by a predeformation w^* of the beam in its natural unstressed state. To the extent that the level of imperfection can reasonably be expected to scale with the structure's size, the amplitude is modeled as proportional to a characteristic length; hence, $w_{\max}^* = \gamma L$, where γ is dimensionless, small, and typically unknown in advance.

With imperfection so modeled, the beam's length in S_0 is

$$s = L + \frac{1}{2}\int_0^{L} w_{,x}^{*2} \,\mathrm{d}x \tag{8}$$

and the change in length from S_0 to S_2 becomes

$$\Delta s = \delta - \frac{1}{2}\int_0^{L} (w_{,x}^2 - w_{,x}^{*2}) \,\mathrm{d}x. \tag{9}$$

Flexure of the beam remains calculated with respect to the curvature of the initially deformed beam [13]. The desired form of the governing equation for finite deflection of an imperfect beam becomes

$$EI(w_{,xxxx} - w_{,xxxx}^*) + EA\left(\varepsilon - \frac{1}{2L}\int_0^{L} (w_{,x}^2 - w_{,x}^{*2}) \,\mathrm{d}x\right)w_{,xx} = 0 \tag{10}$$

subject to the same boundary conditions as equation (7). Several special cases are discussed in the following sections to demonstrate the applicability and limitations of the various buckling models that reduce from equation (10), and that can be applied to micromechanical structures.

2.1. Linear model without imperfection

In the most straightforward case [14], non-linearity and imperfections are not considered, and equation (10) simplifies to $EIw_{,xxxx} + EA\varepsilon w_{,xx} = 0$. Solution of the associated eigenvalue problem provides

$$P_c = EA\frac{\delta}{L_c} = \frac{4\pi^2 EI}{L_c^2} \tag{11}$$

and the strain $\varepsilon = \delta/L$ that buckles a beam of critical length is determined. In the linear theory, the beam remains undeflected until δ_c is reached, and although $w_{\max}$ is undetermined, the profile of the beam at critical loading is

$$w = \frac{1}{2}w_{\max}\left(1 - \cos\frac{2\pi x}{L}\right). \tag{12}$$

The prediction of this model is illustrated in figure 2(a) by the bold line, where the equilibrium $w_{\max} = 0$ is stable for $\delta < \delta_c$ and is unstable for all larger values.

2.2. Linear model with imperfection

When the net imperfection is modeled by predeformation in S_0, the governing differential equation

$$EIw_{,xxxx} + EA\varepsilon w_{,xx} = EIw_{,xxxx}^* \tag{13}$$

is inhomogeneous. For simplicity, the predeformation is chosen as

$$w^* = \frac{1}{2}\gamma L\left(1 - \cos\frac{2\pi x}{L}\right) \tag{14}$$

to the extent that postbuckling behavior is governed largely by the component of the predeformation that is proportional to the lowest buckling mode [14, 15]. The error associated with neglecting the higher-order components of w^* is judged to be small for treatment of initial postbuckling.

By substituting equations (12) and (14) into equation (13), the dependence of the beam's peak amplitude on length becomes

$$w_{\max} = \begin{cases} \text{undetermined} & \text{if } \delta = \delta_c \\ \frac{\gamma L}{1 - \varepsilon A L^2/4\pi^2 I} & \text{otherwise} \end{cases}. \tag{15}$$

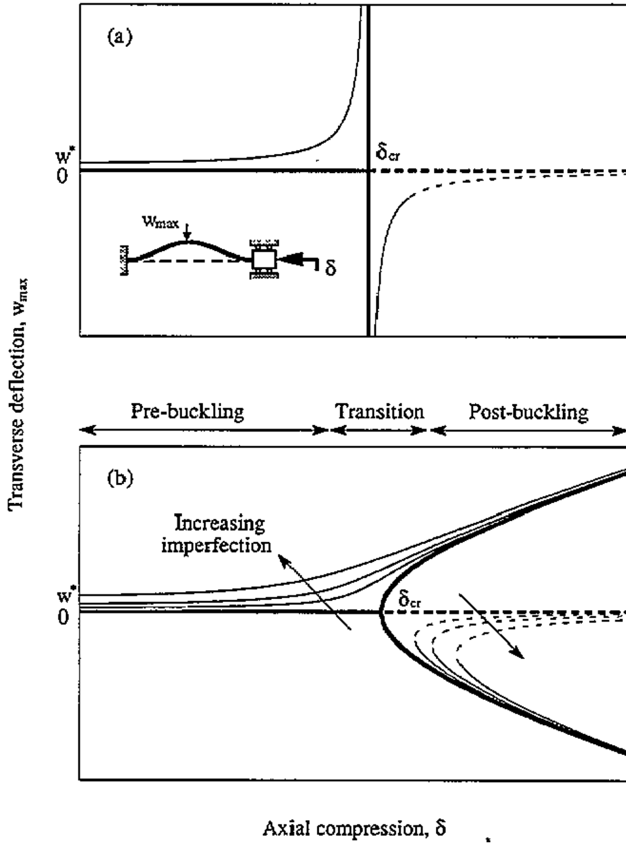

Figure 2. Qualitative behavior in the prebuckling, transition, and postbuckling ranges based on (a) linear and (b) non-linear models. In each diagram, stable (unstable) solutions are shown by solid (dashed) lines, and branches for ideal (imperfect) geometry and loading are shown by bold (thin) lines.

The model predicts a smooth increase of amplitude for loads below δ_c, as depicted by the thin solid line in figure 2(a) where $\gamma = 0.005$. Even for that seemingly small imperfection, the buckling behavior and growth of the out-of-plane amplitude are altered, particularly near δ_c. In place of the buckling 'point', it becomes useful in the present case to consider instead a region of transition from small to large deflections. To the extent that this model is linear, however, it remains incapable of predicting the observed postbuckled amplitudes.

2.3. Non-linear model without imperfection

By substituting equation (12) into equation (7), the relationship between w_{max} and L becomes

$$w_{max} = \begin{cases} 0 & \delta < \delta_c \text{ prebuckling} \\ 0 & \delta = \delta_c \text{ bifurcation} \\ 0 \text{ and } \pm\sqrt{\frac{4\varepsilon L^2}{\pi^2} - \frac{16I}{A}} & \delta > \delta_c \text{ postbuckling} \end{cases} \quad (16)$$

Although the beam is compressed, it does not deflect transversely until the end's displacement reaches δ_c, and at that point the number of equilibrium states changes from one to three. In figure 2(b), the bold lines for $\delta > \delta_c$ depict the two stable equilibria w^+_{max} (buckled up) and w^-_{max} (down) as in equation (16). Subject to a small disturbance, beams in the unstable (dashed) trivial state for $\delta > \delta_c$ will 'jump' to either of the stable configurations.

2.4. Non-linear model with imperfection

The most general case of equation (10) for finite deformation of a slightly imperfect structure is considered exclusively in the following. By specifying the linear-buckling mode in equations (12) and (14) as the shape function for both w and w^*, the fourth-order, non-linear equation (10) is reduced to the simpler algebraic relation

$$w^3_{max} + \left(16\frac{I}{A} - \frac{4}{\pi^2}L^2\varepsilon - \gamma^2 L^2\right) w_{max} - 16\frac{I}{A}\gamma L = 0. \quad (17)$$

Re-writing this as $w^3_{max} + a w_{max} + b = 0$, the solution is given in closed form by

$$w_{max} = \begin{cases} \sqrt[3]{-b/2 + \sqrt{\beta}} - \sqrt[3]{b/2 + \sqrt{\beta}} & \beta > 0 \\ 2\sqrt{-a/3}\cos(\theta/3 + 2(n-1)\pi/3) & \text{otherwise} \end{cases} \quad (18)$$

where $\beta = (b^2/4 + a^3/27)$, $\theta = \cos^{-1}(3b/(2a\sqrt{-a/3}))$, and $n = 1$, 2, or 3. The physical value of w_{max} is taken as the real root of equation (18), and the solution so constructed exactly satisfies equation (10).

For given values of the parameters ε, γ and I/A, the amplitude in the prebuckling, transition, and postbuckling regions can be evaluated in equation (18) as a function of L. In figure 2(b), the growth of w_{max} predicted by the present model is smooth, continuous, and monotonic near δ_c. The width of this transition region grows with imperfection and vanishes in the limit $\gamma = 0$ for ideal loading and geometry. The maximum deviation of the present model's predictions and those from ones based on idealized conditions occurs in the near-critical loading region. In fact, that is the most important range insofar as determination of thin-film stress is concerned, as borne out by the discussed sensitivity of ε to measurement errors in L_c.

3. Fabrication and measurement

An array of beams with lengths between 30 and 140 μm was fabricated through conventional bulk micromachining. An SiO_2 layer was thermally grown at 1100 °C on a polished single-crystal silicon substrate with (100) orientation, and it was patterned by ion milling. The substrate was etched isotropically with a 5/15/1 mixture of $CH_3COOH/HNO_3/HF$ solution at room temperature [16]. When relieved from the substrate, the completed oxide beams were suspended above a cavity. Because the substrate was several hundred times thicker than the oxide film, neighboring beams in the array were assumed to be uncoupled in their

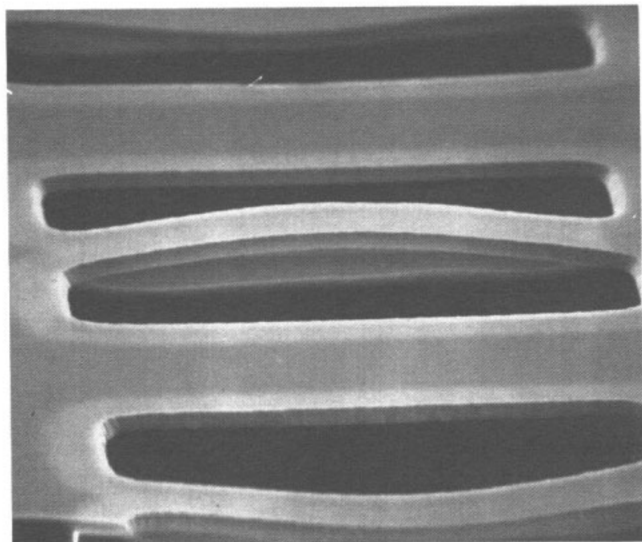

Figure 3. SEM photograph of an 88 μm clamped–clamped beam.

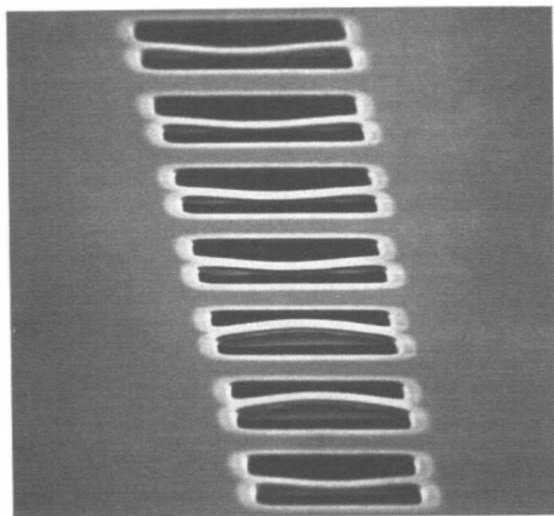

Figure 4. A portion of the microbeam array.

out-of-plane deflections. Although the isotropic etchant did undercut the ends of each beam by approximately a half-width, the boundary was judged sufficiently rigid to be modeled as clamped. An SEM photograph of a typical microbeam in the postbuckled state, 88 μm long, 15 μm wide, and 2 μm thick is shown in figure 3, and seven such beams in the range 84–108 μm are shown, in figure 4.

A non-contact interferometric profilometry system was used to characterize the deflected amplitude and shape of the beams. The fringe pattern generated by interference between the light reflected from a reference surface and from a target microbeam provided the three-dimensional surface profile. In turn, the fringe pattern was digitized by a 256 $\times$ 256 element CCD camera, and the data set was reconstructed to obtain the beam's

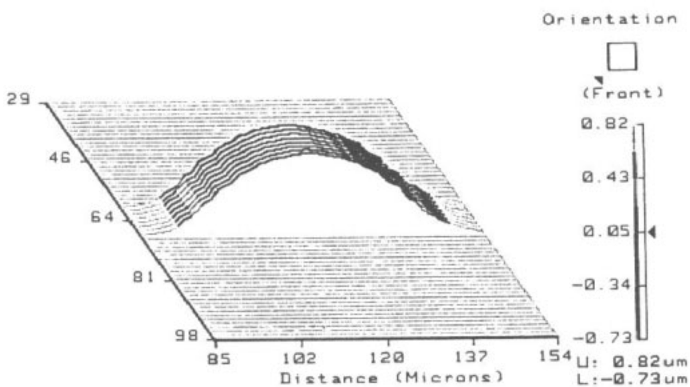

Figure 5. Measured three-dimensional profile of a buckled 68 μm beam, for which $w_{max} = -1.55$ μm. The profile is inverted for clarity.

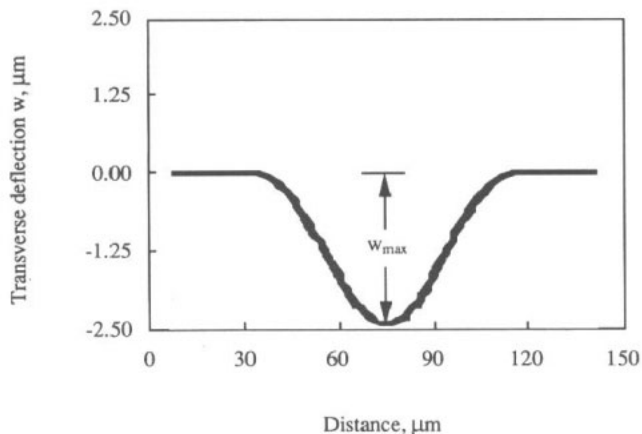

Figure 6. Measured x-axis profile of an 80 μm beam.

profile. In the present case, the imaged field of view with a 40$\times$ objective lens was approximately 256 μm by 256 μm. The cavities on each side of the micromachined beams were masked in software to prevent singularity in the measurement along the boundary of each beam. The profile of a 68 μm beam measured in this manner is shown in figure 5, and the peak amplitude was obtained by sectioning the data along the x-axis generator as depicted in the measurement of figure 6. These measurements further support the modeling assumptions of a clamped boundary, and of specifying the first linear-buckling mode as the shape function for postbuckling.

4. Discussion

Deflection measurements for beams of twenty different lengths and from six different arrays on the same wafer illustrate the variation of out-of-plane amplitude with length for δ specified at prebuckling, transition, and postbuckling levels. The data points in figure 7 denote the average measured values, and the vertical bars indicate the highs and lows that were recorded over the ensemble of measurements. Sets of beams were fabricated with rectangular or trapezoidal cross-sections. In each case, the dependence of w_{max} on the load is continuous, and is more gradual than the sharp

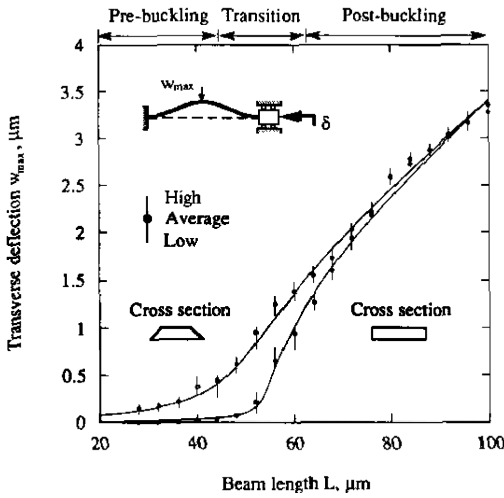

Figure 7. Comparison of the measured and predicted results for w_{max}. The parameters in equation (17) are determined by calibrating the model (solid line) to the data points (○, ●). Measured results are taken over six beam arrays.

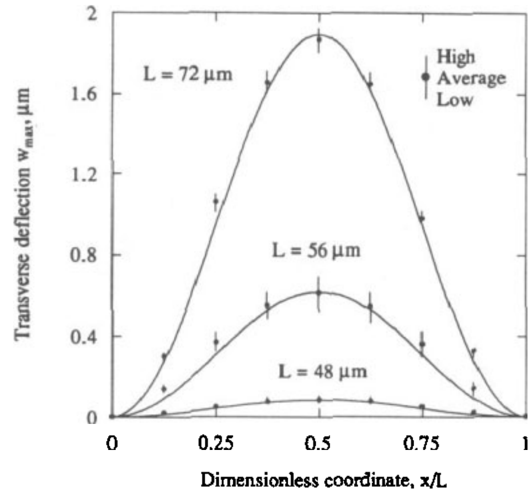

Figure 8. Comparison of measured and predicted profiles of beams with lengths in the prebuckling (48 μm), transition (56 μm), and postbuckling (72 μm) regions. The measured results are taken over six beams.

bifurcation within the 40–60 μm range that is predicted by simpler buckling models. This behavior is attributed to the presence of initial structural imperfections, and is captured by w^* in equation (10).

The model is calibrated to the measurements by a least-squares fit of equation (17). With the as-yet-undetermined ε, γ, and I/A treated as the degrees of freedom, the error

$$\eta = \sum_{i=1}^{N}((w_{max})_i - (\hat{w}_{max})_i)^2 \qquad (19)$$

is minimized through Powell's method over beams with identical cross section and of N different lengths L_i. Here $(w_{max})_i$ represents the model's prediction, and $(\hat{w}_{max})_i$ is the average measured value. By identifying I/A in this manner, the experimental errors from measuring thickness and width of the beams can be reduced, particularly if the cross-section is irregular. The best fit of the model to the data for a rectangular cross-section in figure 7 is obtained with the residual thermal strain $\varepsilon = 4.1 \times 10^{-3}$, the geometric parameter $I/A = 0.31$ μm^2, and the net imperfection $\gamma = 3.7 \times 10^{-4}$. For a beam of length 100 μm and thickness 2 μm, for instance, this value of γ corresponds to a net imperfection of approximately 1.9% of the beam's thickness. For this value of ε, equation (2) provides $L_c = 56$ μm, at which $w_{max} = 0.58$ μm, some 30% of the beam thickness. The deflections predicted by the model with these parameters are also shown in figure 7, and as can be seen, the model captures the data in each of the three load ranges.

For the case of trapezoidal cross-sections, the imperfection level becomes larger. From profilometry and inspection of SEM photographs, the trapezoidal cross-sections were measured to be approximately 3 μm wide on the upper surface and 15 μm wide on the lower. From the deflection measurements and model results as indicated in figure 7, the initial imperfection level, residual strain, and geometric constant are found to be 3.2×10^{-3}, 3.8×10^{-3} and 0.27 μm^2, respectively. Therefore, the imperfection level in this case was nearly ten times greater than for the rectangular cross-section, while the measured residual strain differed by only 6% since the oxide was grown at the same time.

With the value of $E = 66$ GPa [17] for the oxide's elastic modulus, the thermal stress in the film becomes 0.27 GPa. By way of comparison with previous results, stress levels calculated from equation (1) of 0.34 GPa [17], and of 0.3 GPa [18], have been reported. If postbuckling and the gradual growth of w_{max} near δ_c are not considered, σ can be overestimated or underestimated as a result of errors in extracting only L_c from the measurements [5]. For instance, by qualitative inspection alone of the beams with rectangular cross-section in figure 7, a value for L_c of 52 μm (at which $w_{max} = 0.2$ μm) could be chosen; calculation in equation (2) then provides $\varepsilon = 4.9 \times 10^{-3}$. That value is some 16% higher than the one determined by using the present technique of fitting the model to the postbuckled deflections. If, on the other hand, L_c is chosen to be 60 μm (where $w_{max} = 1.02$ μm), the value estimated by equation (2) for ε is only 90% of the present value. In this sense, the ambiguity in identifying the critical load condition is reduced with the present technique to the extent that ε is found by a least-squares fit of the model to the data over a range of L.

The stress estimate obtained through the companion technique of Lin and Pugacz-Muraszkiewicz [7] is based on the postbuckled load P_2. As discussed, $P_2 < P_1$, and is not related to ε through the simple relation (1). For the case of a 100 μm beam that deflected at 3.25 μm, $P_1 = 8$ mN and $P_2 = 4.3$ mN. Use of P_2 in the place of P_1 in equation (2) underestimates σ by some 46%, underscoring the need for inclusion of the postbuckling behavior in the stress calculation.

Once ε, I/A, and γ are determined, both the amplitude and shape of the postbuckled micromachined beams can be predicted. As shown in figure 8, the

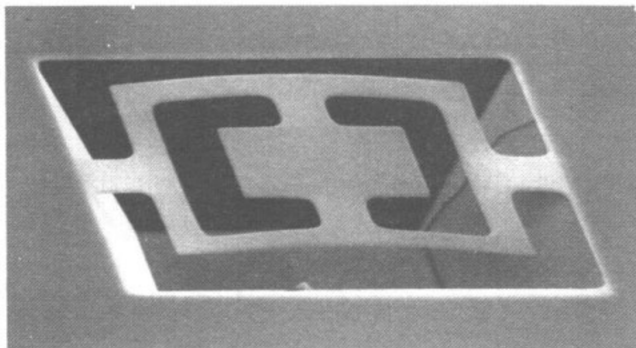

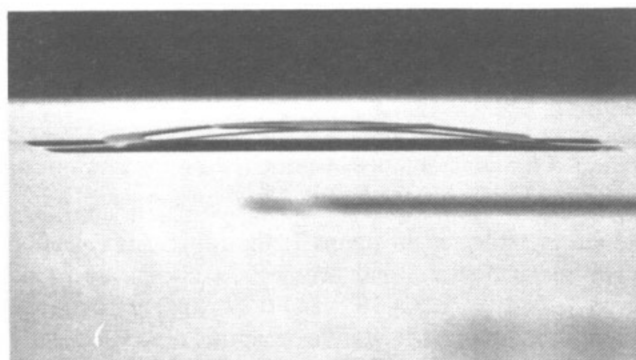

Figure 9. Gimbal spring with one translational (out-of-plane) and two rotational (pitch and roll) degrees of freedom. The postbuckled shape allows attachment to the central platform.

measured beam profiles support the predicted ones in each buckling region. The model can be applied to predict the deflection amplitude for beams with different cross-sections and lengths when ε and γ are known. To the extent that the model can predict the postbuckled amplitude, micromachined structures can be designed with specified out-of-plane geometry. One such example is the three-degree-of-freedom gimbal spring that is shown in figure 9 [19].

5. Summary

The contributions of this study include an improved model and measurement technique for determining residual thin-film stress based on the buckling of diagnostic micromachined structures, and for predicting in advance their finite postbuckled amplitude. The residual strain level is found by calibrating the model against the measured data, so that the width, thickness, and cross-section of the beam need not be measured directly. Further, the method does not require a particularly high resolution of beam length in the array, and so the array can comprise fewer elements.

Buckling behavior in the transition region is sensitive to the net level of imperfection, and cannot be predicted with fidelity by models that assume idealized geometry and loading. This point has implications for the accurate prediction of residual stress when the beam of critical length L_c, which in idealized models demarcates the 'unbuckled' beams from the 'buckled' ones, is to be identified.

Acknowledgments

This material is based (in part) upon work supported by the National Science Foundation under grant number ECD-8907068.

References

[1] Ohring M 1992 *The Materials Science of Thin Films* (San Diego, CA: Academic)

[2] Nix W D 1989 Mechanical properties of thin films *Metall. Trans.* A **20** 2217–45

[3] Cullity B D 1972 *Introduction to Magnetic Materials* (Reading, MA: Addison-Wesley)

[4] Thornton J A and Hoffman D W 1989 Stress-related effects in thin film *Thin Solid Films* **171** 5–31

[5] Guckel H, Randazzo T and Burns D W 1985 A simple technique for the determination of mechanical strain in thin films with application to polysilicon *J. Appl. Phys.* **57** 1671–5

[6] Howe R T and Muller R S 1983 Polycrystalline silicon micromechanical beams *J. Electrochem. Soc.* **130** 1420–3

[7] Lin S C H and Pugacz-Muraszkiewicz I 1972 Local stress measurement in thin thermal SiO_2 films on Si substrates *J. Appl. Phys.* **43** 119–25

[8] Wilmsen C W, Thompson E G and Meissner G H 1972 Buckling of thermally-grown SiO_2 thin films *IEEE Trans. on Electron Devices* **ED-19** 122

[9] Guckel H, Burns D, Rutigliano C, Lovell E and Choi B 1992 Diagnostic microstructures for the measurement of intrinsic strain in thin films *J. Micromech. Microeng.* **2** 86–95

[10] Jaccodine R J and Schlegel W A 1966 Measurement of strains at Si-SiO_2 interface *J. Appl. Phys.* **37** 2429–34

[11] Mehregany M, Howe R T and Senturia S D 1987 Novel microstructures for the in situ measurement of mechanical properties of thin films *J. Appl. Phys.* **62** 3579–84

[12] Bouwstra S, Kemna P and Legtenberg R 1989 Thermally excited resonating membrane mass flow sensor *Sensors Actuators* **20** 213–23

[13] Timoshenko S and Woinowsky-Krieger S 1959 *Theory of Plates and Shells* (New York: McGraw-Hill)

[14] Dym C L 1974 *Stability Theory and Its Application to Structural Mechanics* (Leyden: Noordhoff)

[15] Hutchinson J W and Koiter W T 1970 Postbuckling theory *Applied Mechanics Reviews* **23** 1353–65

[16] Kern W and Deckert C A 1978 Chemical etching *Thin Film Processes* ed J L Vossen and W Kern (New York Academic)

[17] Runyan W R and Bean K E 1990 *Semiconductor Integrated Circuit Processing Technology* (Reading, MA: Addison-Wesley)

[18] Wolf S and Tauber R N 1986 *Silicon Processing* (Sunset Beach, CA: Lattice)

[19] Wickert J A, Lambeth D N and Fang W 1991 Towards a micromachined dual slider and suspension assembly for contact recording *ASME Special Publication STLE/ASME Tribology Conf. (St Louis, MO, 1991)*; TRIB vol 3, pp 27–39